Spring 2014

Investigating TeV Gamma Ray Propagation: Establishing Blazar/Absorber Sightline Properties

Julie Davis
University of Colorado Boulder

Investigating TeV Gamma Ray Propagation: Establishing Blazar/Absorber Sightline Properties

Julie D. Davis

University of Colorado Boulder

Department of Astrophysical and Planetary Sciences

Thesis Advisor: Dr. John Stocke

Defended April 3rd, 2014

Defense Committee

Dr. John Stocke, Astrophysical and Planetary Sciences

Dr. Mark Rast, Astrophysical and Planetary Sciences

Dr. Steven Pollock, Physics

Dr. Charles Danforth, Astrophysical and Planetary Sciences

Investigating TeV Gamma Ray Propagation: Establishing Blazar/Absorber Sightline Properties

Julie D. Davis

University of Colorado at Boulder

julie.davis@colorado.edu

ABSTRACT

The standard model for propagation of gamma rays from very high energy (VHE, E≥100 GeV) blazars through the universe requires an understanding of the diffuse extragalactic background light (EBL). Due to photon-photon collision and pair production from gamma ray/infrared photon interaction in the intergalactic medium, we expect a redshift horizon beyond which gamma rays from these sources are significantly attenuated. Two TeV-bright blazars examined in this project pose a problem to the horizon hypothesis due to their substantial redshifts. Given that an unusually low density of foreground galaxies could account for the unexpected TeV observations, this project establishes estimates of foreground galactic populations by using HI (Lyman α) absorbers seen in HST/COS far-UV spectra of PG1424+240 and 3C66A as proxies for counting individual galaxies along the lines of sight. Comparisons to global averages of both number density $d\mathcal{N}/dz$ of absorbers and the luminosity function space density constant ϕ^* result in a conclusion of higher-than-average foreground galactic populations for both PG1424+240 and 3C66A, requiring reevaluation of either the gamma-ray propagation model or the EBL model.

1. Introduction

1.1. Extragalactic Background Light

Extragalactic background light (EBL) is the optical to infrared regime of diffuse extragalactic background radiation. The EBL is the sum of emitted starlight across the history of the universe, including light directly emitted by stars and light reprocessed by interstellar dust. We assume the bulk of EBL light is a product of galaxy formation, evolution, and current emission, though small contributions from cluster-originating diffuse radiation and faint sources may also be included (Kneiske et al. 2010).

The EBL is an important consideration in high energy astronomy. Gamma rays propagating from very high energy (VHE, E≥100 GeV) sources can interact with low energy EBL photons to produce electron-positron pairs. The intrinsic spectrum of a VHE source is thus damped by an exponential such that $F_{obs}(E) = F_{int}(E) \times e^{-\tau(E)}$, where $\tau(E)$ is opacity as a function of the EBL spectral energy distribution (SED) (Aharonian et al. 2006). This process significantly attenuates high energy fluxes, creating a redshift horizon beyond which we expect to see little to no gamma ray flux due to increased opacity from the intervening EBL material. For a gamma ray energy of 1 TeV, most EBL models predict $\tau = 1$ occurs around z∼0.1. However, a number of VHE sources detected by Cherenkov telescopes such as FERMI, VERITAS, and MAGIC have firm redshift lower limits beyond the redshift horizon predicted by many models of the EBL (Kneiske et al. 2002, Primack et al. 2005, Stecker et al. 2006). Two of these sources, PG1424+240 and 3C66A, are TeV-bright sources at redshifts greater than 0.4 (Furniss et al. 2013a,b) and thus in conflict with predicted redshift horizons.

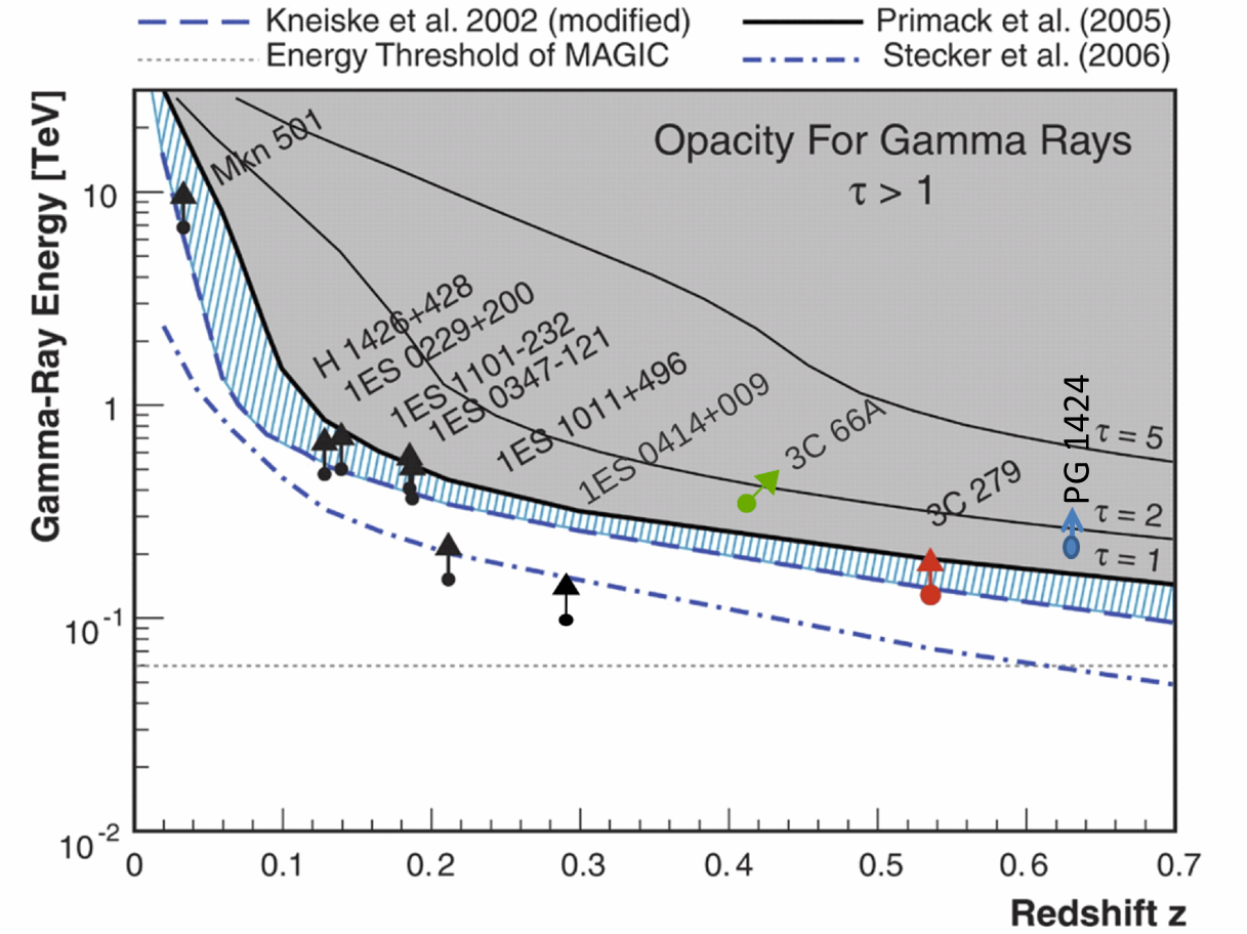

Fig. 1.— Models of the extragalactic background light opacity to gamma radiation with various blazars plotted (figure modified from Kneiske & Dole 2010). Blazars 3C66A and PG1424+240 cross into the $\tau \sim 1$ region, where more attenuation was expected than observed.

1.2. Gamma Ray Physics

As seen in Stecker & De Jager (1993), consider a TeV gamma ray of energy $E(z) = (1+z)E$ and a soft photon of energy $\epsilon(z) = (1+z)\epsilon$, where E and ϵ are the photon energies at $z = 0$. The threshold for photon/photon pair production is reached when $E\epsilon(1+z)^2(1-\cos\theta) > 2\left(mc^2\right)^2$, where E$\epsilon$ is the product of the two photon energies and θ is the angle between the photon paths. The cross section is given by:

$$\sigma\left[E(z), \epsilon(z), x\right] = 1.25 \times 10^{-25}\left(1-\beta^2\right)\left[2\beta\left(\beta^2-2\right) + \left(3-\beta^4\right)\ln\left(\frac{1+\beta}{1-\beta}\right)\right]\text{cm}^2 \quad (1)$$

Where $\beta = \left\{1 - 2\left(mc^2\right)^2 / \left[E\epsilon(1+z)^2(1-\cos\theta)\right]\right\}^{1/2}$. For a TeV gamma ray, the cross section maximizes when the soft photon falls in the infrared regime. For E$\sim$1 TeV, $\epsilon \sim$0.5 eV, which corresponds to a $\sim$2 μm photon wavelength, or K-band. At higher gamma ray energies, the soft photon energy reaches further into the infrared.

$$\epsilon\left(E\right) \simeq \frac{2\left(mc^2\right)^2}{E} \simeq 0.5\left(\frac{1\mathrm{TeV}}{E}\right)\mathrm{eV} \tag{2}$$

1.3. Ultraviolet Spectroscopy as an EBL Probe

Due to contamination from foreground zodiacal and galactic light, the EBL is difficult to measure directly. The global distribution of the background radiation is likely inhomogeneous, as we suspect the bulk of the EBL photons causing pair production are supplied by galaxies in the foreground of VHE sources. Since galaxy distributions are inhomogeneous, the EBL radiation field may vary in density and thus explain anomalously high redshift TeV source detections. To probe the potential EBL sources along the line of sight, we make use of ultraviolet spectroscopy of blazars. Blazars (radio-loud active galactic nuclei with a relativistic jet oriented towards Earth) have flat power law continuum spectra with few intrinsic emission or absorption lines (Stocke et al. 2011), making them ideal for examining absorption systems. The Lyman forest and metal ion absorptions give clues as to the number and distribution of absorbers along the line of sight, and thus an estimate of EBL levels. This method is, however, sensitive to the redshift of the blazar itself. The redshifts of the two targets in this paper have recently been constrained by Furniss et al. (2013a, 2013b). These two papers establish firm lower limits and statistical upper limits on the distance of both PG1424+240 and 3C66A through examination of HI absorbers. Detection of absorption features up to a given redshift indicate strict lower limits to the blazar redshift. Statistical redshift upper limits were obtained by comparing predicted numbers of absorption lines on a given redshift interval to non-detections beyond the lower limit redshift. 3C66A presented non-detection of absorbers beyond $z \sim$0.3347 and statistically rules out $z \geq$0.444 at 99.9% confidence. PG1424+240 presented a non-detection of absorbers beyond $z \sim$0.6035 and statistically rules out $z \geq$0.75 with 95.5% confidence.

2. Observations

Blazar 3C66A was first observed at VHE levels at the Crimean Astrophysical Observatory with the GT-48 atmospheric Cerenkov detector via electron-photon showers between 1996 and 1998. For energies greater than 1 TeV, a flux of $(3.0 \pm 0.9) \times 10^{-11}$ photons cm^{-2} s^{-1} was measured (Neshpor et al. 1999). More recently it was measured by VERITAS at an average flux above 200 GeV of $(3.9 \pm 1.6) \times 10^{-12}$ photons cm^{-2} s^{-1} (Acciari et al. 2009), though it is observed to be highly variable. PG1424+240 was first observed at VHE energy levels by the imaging atmospheric Cerenkov detector MAGIC in 2009. Fluxes at TeV energies were measured by VERITAS at $(5.1 \pm 1.4) \times 10^{-11}$ photons cm^{-2} s^{-1} (Acciari et al. 2010).

For ulraviolet spectroscopy, targets PG1424+240 and 3C66A were observed under Hubble Space Telescope (HST) program 12612 (PI: Stocke) as part of a project using flaring blazars to probe absorption in the intervening intergalactic medium (IGM). PG1424+240 and 3C66A are included in a collection of ∼200 targets monitored by a network of robotic telescopes: the 0.76m Katzman Automatic Imaging Telescope (KAIT) at Lick Observatory; the 0.4m NF/ Observatory in Silver City, New Mexico; and the Small and Moderate-Aperture Remote Telescope System (SMARTS) on Cerro Tololo. The targets were observed approximately every two weeks during the target visibility period of 6-8 months. When a target brightened to V $<$ 15.5, observing cadences were increased. Flaring targets of sufficient interest to IGM/quasar absorption line science showing systematic brightening (V $<$ 14.5) for four or five consecutive observations were then observered by HST/COS, resulting in observations two to three weeks later (Stocke et al. 1998).

PG1424+240 was observed on April 19th, 2012 after optical photometry indicated sufficient magnitude increase to trigger a five-orbit HST Cosmic Origins Spectrograph (COS) observation. Medium resolution (R$\equiv \lambda/\Delta\lambda \sim$ 18,000) FUV gratings G130M (1135 $< \lambda <$ 1450 Å, 6.4 ks) and G160M (1400 $< \lambda <$ 1795 Å, 7.9 ks) were used to obtain the spectrum, which was then reduced using standard IDL procedures as detailed in Danforth et al. (2010). 3C66A was observed by HST for five orbits on November 1st, 2012 again using the medium resolution COS G130M and G160M gratings. Three additional orbits under HST program 12863 (PI: Furniss) were taken on November 8th, 2012. Corrections and reductions were performed as outlined in Danforth et al. (2013) and Furniss et al.(2013).

3. Line Identification and Measurement

Line identification and measurement were performed following the procedure outlined in Danforth et al. (2014). Starting with the strongest lines, Lyα was the initial identification assumption. For strong absorbers ($\mathcal{W} \geq 150$ mÅ), a Lyα line should be accompanied by higher order line detections at the same redshift. In addition, the higher order line should approximate the correct equivalent width given that Lyman optical depths obey ratios between the orders (τ[lyα]/τ[lyβ] ≤ 6.2). Therefore, a positive Lyman identification was made when a line was found at the correct wavelength and exhibited a width consistent with the ratio of optical depth. After this iterative process, the remaining weak, unidentified lines were assumed to be Lyα unless otherwise proven. Comparisons to interstellar line databases identified ISM absorptions, and further analysis of weak lines with properties such as doublet structures revised some identifications to metal ions of strong absorbers. Given that the density of Lyman absorption lines increases dramatically in the bluer wavelengths of the spectrum, the process worked from red to blue until all lines were identified as Lyman systems or not Lyα. The process then started over with the initial assumption moved to Lyβ to cover the most redshifted strong absorbers.

Equivalent widths and column densities were calculated using IDL routines (Danforth et al. 2014) for voigt fitting and curve of growth. An automatic line-finding and measurement algorithm was used to characterize the spectra. For absorbers with both neutral hydrogen and metal ions present, voigt fitting and curves of growth were also measured without the automatic fitting algorithm. Several absorbers consisted of multiple velocity components, indicating likely blending in the strongest lines and thus necessitating the fitting of multiple voigt profiles to certain absorbers. If higher order lines exhibited easily-differentiable components, the Lyα and β lines could be fit with some degree of confidence. If the the lines were well blended or asymmetric, more ambiguity was introduced to the voigt fitting, necessitating more statistical uncertainty analysis. In addition, when multiple Lyman orders were detected for a single absorber, a curve of growth was constructed using IDL routines to corroborate measurements of equivalent width and column density from profile fitting to increase accuracy statistics. 3C66A exhibits 41 distinct absorber systems and PG1424+240 exhibits 64. Tables 1 and 2 present the results of these measurements.

Table 1. Extragalactic Absorption Systems Toward 3C 66A

Species	$z_{\rm abs}$	W_r (mÅ)	b (km s^{-1})	log N (N in cm^{-2})	SL (σ)
$z = 0.00188 \pm 0.00013$, $\Delta v = 39$ km s^{-1}					
CIV 1548	0.00188	129 ± 26	20 ± 4	13.64 ± 0.07	8.6
CIV 1550	0.00188	115 ± 29	28 ± 5	13.84 ± 0.09	6.6
SiIII 1206	0.00186	80 ± 32	23 ± 4	12.67 ± 0.16	6.3
Lya 1215	0.01991	57 ± 12	25 ± 7	13.08 ± 0.11	7.7
Lya 1215	0.02028	52 ± 14	43 ± 11	13.01 ± 0.09	5.4
Lya 1215	0.02730	110 ± 7	19 ± 2	13.47 ± 0.04	16.6
Lya 1215	0.04254	88 ± 9	26 ± 2	13.29 ± 0.04	10.8
Lya 1215	0.04424	75 ± 13	48 ± 7	13.18 ± 0.06	6.6
Lya 1215	0.05122	267 ± 4	39 ± 3	13.89 ± 0.04	25.8
Lya 1215	0.05150	226 ± 26	45 ± 5	13.75 ± 0.05	20.6
Lya 1215	0.05341	75 ± 8	27 ± 4	13.21 ± 0.05	8.6
$z = 0.06748 \pm 0.00068$, $\Delta v = 192$ km s^{-1}					
Lya 1215	0.06707	155 ± 62	20 ± 2	13.69 ± 0.04	16.0
Lya 1215	0.06748	832 ± 11	28 ± 1	17.64 ± 0.12	75.4
SiIV 1393	0.06743	37 ± 53	20 ± 9	12.66 ± 0.37	2.9
SiIV 1402	0.06754	18 ± 10	5 ± 1	12.70 ± 0.19	2.1
SiIII 1206	0.06737	102 ± 23	30 ± 3	12.77 ± 0.08	9.0
Lya 1215	0.07974	176 ± 12	33 ± 2	13.65 ± 0.02	17.0
Lya 1215	0.08020	46 ± 16	40 ± 11	12.96 ± 0.11	4.1
Lya 1215	0.08346	100 ± 13	28 ± 3	13.35 ± 0.04	9.6
Lya 1215	0.08872	384 ± 16	34 ± 1	14.32 ± 0.03	28.0
Lya 1215	0.10824	60 ± 11	29 ± 4	13.10 ± 0.06	7.5
$z = 0.11550 \pm 0.00029$, $\Delta v = 77$ km s^{-1}: $b_{\rm HI} = 33 \pm 1$, log $N_{\rm HI} = 14.21 \pm 0.04$					
Lya 1215	0.11550	351 ± 10	42 ± 1	14.08 ± 0.01	38.1
Lyb 1025	0.11546	137 ± 71	51 ± 12	14.35 ± 0.22	4.4
Lya 1215	0.12027	47 ± 11	31 ± 7	12.98 ± 0.07	5.8
$z = 0.13062 \pm 0.00013$, $\Delta v = 35$ km s^{-1}					
Lya 1215	0.13051	53 ± 12	34 ± 6	13.03 ± 0.08	5.7
Lyb 1025	0.13062	60 ± 14	58 ± 18	13.94 ± 0.10	3.1
Lya 1215	0.14187	107 ± 16	63 ± 6	13.33 ± 0.05	9.3
$z = 0.15157 \pm 0.00019$, $\Delta v = 50$ km s^{-1}: $b_{\rm HI} = 21 \pm 1$, log $N_{\rm HI} = 14.14 \pm 0.13$					
Lya 1215	0.15157	236 ± 25	28 ± 2	13.90 ± 0.05	35.8
Lyb 1025	0.15158	85 ± 28	43 ± 14	14.12 ± 0.14	7.3
OVI 1032	0.15155	38 ± 19	33 ± 11	13.51 ± 0.18	3.3
OVI 1038	0.15147	47 ± 44	60 ± 16	13.90 ± 0.31	3.4
$z = 0.15184 \pm 0.00020$, $\Delta v = 52$ km s^{-1}: $b_{\rm HI} = 23 \pm 8$, log $N_{\rm HI} = 14.04 \pm 0.25$					
Lya 1215	0.15184	244 ± 10	28 ± 4	13.94 ± 0.10	37.3
Lyb 1025	0.15186	67 ± 28	33 ± 12	14.02 ± 0.18	6.5
Lya 1215	0.15205	172 ± 83	56 ± 17	13.57 ± 0.22	18.6
Lya 1215	0.16240	114 ± 8	57 ± 5	13.37 ± 0.03	11.3
Lya 1215	0.16964	49 ± 8	26 ± 4	13.01 ± 0.06	7.2
$z = 0.17519 \pm 0.00014$, $\Delta v = 36$ km s^{-1}: $b_{\rm HI} = 30 \pm 4$, log $N_{\rm HI} = 13.72 \pm 0.09$					
Lya 1215	0.17519	172 ± 13	44 ± 3	13.60 ± 0.03	16.8
Lyb 1025	0.17516	34 ± 15	17 ± 6	13.72 ± 0.15	3.0
$z = 0.17563 \pm 0.00031$, $\Delta v = 79$ km s^{-1}: $b_{\rm HI} = 28 \pm 1$, log $N_{\rm HI} = 14.53 \pm 0.04$					
Lya 1215	0.17563	377 ± 11	41 ± 1	14.15 ± 0.01	37.7

Table 1—Continued

Species	$z_{\rm abs}$	W_r (mÅ)	b (km s^{-1})	log N (N in cm^{-2})	SL (σ)
Lyb 1025	0.17563	165 ± 29	51 ± 5	14.45 ± 0.06	9.0
Lyg 972	0.17565	70 ± 1	25 ± 1	14.55 ± 0.01	3.1
Lya 1215	0.18942	83 ± 12	40 ± 4	13.23 ± 0.05	8.9
Lya 1215	0.22820	34 ± 4	10 ± 6	12.89 ± 0.13	3.3
Lya 1215	0.22859	182 ± 20	52 ± 5	13.61 ± 0.04	11.8
Lya 1215	0.23408	98 ± 17	28 ± 4	13.34 ± 0.06	8.4
$z = 0.24226 \pm 0.00038$, $\Delta v = 90$ km s^{-1}: $b_{\rm HI} = 36 \pm 6$, log $N_{\rm HI} = 14.55 \pm 0.26$					
Lya 1215	0.24226	457 ± 27	60 ± 3	14.16 ± 0.02	29.2
Lyb 1025	0.24213	96 ± 53	61 ± 16	14.16 ± 0.19	7.3
Lyb 1025	0.24247	84 ± 30	47 ± 11	14.10 ± 0.14	7.3
OVI 1032	0.24256	152 ± 14	29 ± 1	14.26 ± 0.04	15.0
OVI 1038	0.24256	95 ± 20	31 ± 3	14.27 ± 0.08	9.2
$z = 0.24268 \pm 0.00019$, $\Delta v = 45$ km s^{-1}: $b_{\rm HI} = 32 \pm 3$, log $N_{\rm HI} = 13.83 \pm 0.04$					
Lya 1215	0.24268	229 ± 25	32 ± 3	13.83 ± 0.04	19.7
OVI 1032	0.24256	152 ± 14	29 ± 1	14.26 ± 0.04	15.0
OVI 1038	0.24256	95 ± 20	31 ± 3	14.27 ± 0.08	9.2
Lyb 1025	0.26111	41 ± 23	32 ± 8	13.79 ± 0.19	3.9
Lya 1215	0.26125	160 ± 40	39 ± 3	13.57 ± 0.10	8.0
Lya 1215	0.29268	63 ± 19	21 ± 8	13.14 ± 0.12	4.5
Lya 1215	0.29906	83 ± 21	27 ± 5	13.26 ± 0.08	5.7
$z = 0.30058 \pm 0.00014$, $\Delta v = 31$ km s^{-1}: $b_{\rm HI} = 26 \pm 3$, log $N_{\rm HI} = 13.67 \pm 0.05$					
Lya 1215	0.30058	168 ± 18	26 ± 3	13.67 ± 0.05	8.5
OVI 1032	0.30054	38 ± 7	50 ± 13	13.51 ± 0.09	3.1
Lya 1215	0.30086	240 ± 24	60 ± 6	13.75 ± 0.04	12.2
$z = 0.32831 \pm 0.00035$, $\Delta v = 78$ km s^{-1}: $b_{\rm HI} = 39 \pm 1$, log $N_{\rm HI} = 14.33 \pm 0.02$					
Lya 1215	0.32831	424 ± 4	44 ± 1	14.24 ± 0.01	14.0
Lyb 1025	0.32828	127 ± 2	43 ± 3	14.32 ± 0.02	11.2
Lyg 972	0.32824	48 ± 26	41 ± 8	14.34 ± 0.18	4.0
Lyd 949	0.32828	33 ± 28	46 ± 11	14.51 ± 0.27	3.4
OVI 1032	0.32824	34 ± 17	47 ± 14	13.46 ± 0.09	3.1
$z = 0.33329 \pm 0.00033$, $\Delta v = 73$ km s^{-1}: $b_{\rm HI} = 37 \pm 6$, log $N_{\rm HI} = 14.28 \pm 0.12$					
Lya 1215	0.33329	399 ± 28	47 ± 2	14.14 ± 0.03	19.5
Lyb 1025	0.33321	116 ± 24	56 ± 4	14.25 ± 0.08	8.8
Lyg 972	0.33318	47 ± 37	50 ± 12	14.32 ± 0.24	3.2
Lyd 949	0.33322	17 ± 26	23 ± 10	14.23 ± 0.38	2.2
$z = 0.33476 \pm 0.00016$, $\Delta v = 36$ km s^{-1}: $b_{\rm HI} = 32 \pm 6$, log $N_{\rm HI} = 13.71 \pm 0.18$					
Lya 1215	0.33476	199 ± 28	36 ± 3	13.71 ± 0.05	11.6
Lyb 1025	0.33473	28 ± 32	27 ± 8	13.62 ± 0.32	3.3

Table 2. Extragalactic Absorption Systems Toward PG 1424+240

Species	$z_{\rm abs}$	W_r (mÅ)	b (km s^{-1})	log N (N in cm^{-2})	SL (σ)
Lya 1215	0.01747	160 ± 11	51 ± 4	13.55 ± 0.03	12.3
Lya 1215	0.01877	410 ± 18	37 ± 1	14.32 ± 0.03	33.1
Lya 1215	0.01917	105 ± 16	73 ± 14	13.32 ± 0.07	6.7
Lya 1215	0.02000	30 ± 7	13 ± 6	12.80 ± 0.09	4.2
Lya 1215	0.03908	41 ± 28	5 ± 3	13.15 ± 0.28	14.4
Lya 1215	0.04117	130 ± 15	45 ± 4	13.45 ± 0.04	11.3
Lya 1215	0.05072	80 ± 23	34 ± 5	13.22 ± 0.09	11.9
Lya 1215	0.06162	92 ± 17	33 ± 5	13.30 ± 0.06	7.9
$z = 0.08328 \pm 0.00016$, $\Delta v = 44$ km s^{-1}: $b_{\rm HI} = 37 \pm 7$, log $N_{\rm HI} = 13.40 \pm 0.17$					
Lya 1215	0.08328	115 ± 58	37 ± 7	13.40 ± 0.17	8.0
	0.08339	53 ± 23	36 ± 16	13.09 ± 0.19	3.7
Lya 1215	0.10584	168 ± 15	38 ± 2	13.60 ± 0.03	14.3
Lya 1215	0.11584	319 ± 25	25 ± 1	14.39 ± 0.08	33.0
Lya 1215	0.11966	103 ± 15	36 ± 4	13.35 ± 0.05	9.8
$z = 0.12136 \pm 0.00058$, $\Delta v = 155$ km s^{-1}: $b_{\rm HI} = 51 \pm 4$, log $N_{\rm HI} = 14.88 \pm 0.04$					
Lya 1215	0.12136	707 ± 45	46 ± 2	15.11 ± 0.10	59.5
Lyb 1025	0.12125	327 ± 3	57 ± 1	14.85 ± 0.01	9.9
OVI 1032	0.12127	117 ± 7	51 ± 4	14.04 ± 0.03	4.7
OVI 1032	0.12154	131 ± 2	24 ± 1	14.20 ± 0.01	7.4
OVI 1038	0.12145	26 ± 5	5 ± 1	13.81 ± 0.15	3.7
OVI 1038	0.12156	133 ± 6	31 ± 4	14.46 ± 0.05	10.8
CIV 1548	0.12117	123 ± 33	26 ± 4	13.58 ± 0.09	7.0
CIV 1550	0.12121	83 ± 11	24 ± 5	13.68 ± 0.06	4.9
SiIII 1206	0.12124	63 ± 24	29 ± 5	12.53 ± 0.13	5.5
Lya 1215	0.12537	29 ± 9	14 ± 7	12.79 ± 0.15	4.0
$z = 0.12753 \pm 0.00016$, $\Delta v = 42$ km s^{-1}: $b_{\rm HI} = 31 \pm 4$, log $N_{\rm HI} = 13.89 \pm 0.06$					
Lya 1215	0.12753	131 ± 24	37 ± 7	13.47 ± 0.08	9.0
Lyb 1025	0.12768	50 ± 5	25 ± 2	13.89 ± 0.05	2.8
$z = 0.12776 \pm 0.00016$, $\Delta v = 43$ km s^{-1}: $b_{\rm HI} = 24 \pm 2$, log $N_{\rm HI} = 13.89 \pm 0.04$					
Lya 1215	0.12776	199 ± 18	23 ± 2	13.84 ± 0.04	16.9
Lyb 1025	0.12768	50 ± 5	25 ± 2	13.89 ± 0.05	2.8
Lya 1215	0.13325	137 ± 14	33 ± 3	13.51 ± 0.04	12.6
Lya 1215	0.13634	82 ± 30	40 ± 6	13.23 ± 0.13	5.4
Lya 1215	0.13706	45 ± 12	22 ± 5	12.97 ± 0.09	5.0
Lya 1215	0.14537	58 ± 7	22 ± 4	13.09 ± 0.06	8.2
$z = 0.14699 \pm 0.00065$, $\Delta v = 170$ km s^{-1}: $b_{\rm HI} = 41 \pm 1$, log $N_{\rm HI} = 15.90 \pm 0.01$					
Lya 1215	0.14699	794 ± 26	55 ± 1	15.02 ± 0.06	66.2
Lyb 1025	0.14684	201 ± 20	25 ± 2	14.76 ± 0.04	15.4
Lyb 1025	0.14718	350 ± 32	33 ± 2	15.29 ± 0.08	23.9
OVI 1032	0.14698	56 ± 17	32 ± 9	13.73 ± 0.15	5.0
OVI 1032	0.14711	60 ± 16	25 ± 8	13.79 ± 0.12	5.9
NV 1238	0.14716	37 ± 13	40 ± 11	13.30 ± 0.18	4.8
CIV 1548	0.14678	110 ± 30	20 ± 9	13.58 ± 0.11	3.9
CIV 1548	0.14703	143 ± 5	13 ± 1	13.81 ± 0.02	6.0
CIV 1550	0.14652	48 ± 17	13 ± 9	13.56 ± 0.16	3.5
CIV 1550	0.14698	245 ± 3	49 ± 1	14.19 ± 0.01	4.4
SiIV 1393	0.14706	43 ± 19	14 ± 5	12.76 ± 0.14	3.7

Table 2—Continued

Species	$z_{\rm abs}$	W_r (mÅ)	b (km s^{-1})	log N (N in cm^{-2})	SL (σ)
SiIII 1206	0.14681	61 ± 13	12 ± 2	12.60 ± 0.07	6.7
SiIII 1206	0.14709	98 ± 5	16 ± 1	12.84 ± 0.03	9.6
Lya 1215	0.14796	136 ± 22	36 ± 2	13.49 ± 0.06	12.8
Lya 1215	0.15868	45 ± 11	44 ± 8	12.94 ± 0.08	5.7
Lya 1215	0.17250	30 ± 28	47 ± 12	12.76 ± 0.29	6.1
Lya 1215	0.17838	146 ± 7	48 ± 2	13.50 ± 0.02	19.7
Lya 1215	0.18035	38 ± 11	46 ± 9	12.87 ± 0.10	5.1
Lya 1215	0.18811	79 ± 17	39 ± 3	13.21 ± 0.08	12.8
Lya 1215	0.18902	34 ± 6	22 ± 5	12.83 ± 0.07	6.1
$z = 0.20061 \pm 0.00067$, $\Delta v = 167$ km s^{-1}: $b_{\rm HI} = 52 \pm 2$, log $N_{\rm HI} = 15.23 \pm 0.07$					
Lya 1215	0.20061	815 ± 17	52 ± 1	15.21 ± 0.09	77.4
Lyb 1025	0.20039	179 ± 14	27 ± 1	14.63 ± 0.03	14.9
Lyb 1025	0.20076	284 ± 16	32 ± 1	14.99 ± 0.03	22.0
Lyg 972	0.20043	103 ± 38	35 ± 7	14.72 ± 0.13	6.8
Lyg 972	0.20078	181 ± 9	36 ± 4	15.05 ± 0.04	11.9
OVI 1038	0.20058	18 ± 11	41 ± 19	13.54 ± 0.32	1.5
CIII 977	0.20061	26 ± 21	7 ± 7	12.72 ± 0.15	3.0
CIII 977	0.20079	119 ± 2	36 ± 4	13.37 ± 0.03	7.8
SiIII 1206	0.20079	24 ± 16	28 ± 8	12.08 ± 0.23	2.9
$z = 0.20640 \pm 0.00020$, $\Delta v = 49$ km s^{-1}: $b_{\rm HI} = 39 \pm 17$, log $N_{\rm HI} = 13.79 \pm 0.21$					
Lya 1215	0.20640	243 ± 10	48 ± 1	13.79 ± 0.01	25.3
Lyb 1025	0.20651	27 ± 20	31 ± 32	13.63 ± 0.41	2.4
Lya 1215	0.21208	18 ± 7	5 ± 1	12.62 ± 0.15	6.5
Lya 1215	0.23090	27 ± 8	18 ± 6	12.74 ± 0.09	4.4
Lya 1215	0.24159	47 ± 10	30 ± 6	12.98 ± 0.07	6.0
$z = 0.25025 \pm 0.00016$, $\Delta v = 38$ km s^{-1}: $b_{\rm HI} = 34 \pm 6$, log $N_{\rm HI} = 13.76 \pm 0.14$					
Lya 1215	0.25025	184 ± 9	30 ± 1	13.70 ± 0.02	23.4
Lyb 1025	0.25031	39 ± 35	38 ± 11	13.76 ± 0.26	3.1
Lya 1215	0.26634	67 ± 12	37 ± 6	13.14 ± 0.06	7.8
Lya 1215	0.28005	74 ± 41	71 ± 12	13.16 ± 0.19	3.8
$z = 0.28536 \pm 0.00027$, $\Delta v = 63$ km s^{-1}					
Lya 1215	0.28519	200 ± 26	20 ± 2	13.93 ± 0.07	19.1
Lya 1215	0.28536	330 ± 15	40 ± 1	14.04 ± 0.02	23.0
Lyb 1025	0.28525	123 ± 36	49 ± 5	14.29 ± 0.11	7.5
Lyg 972	0.28524	38 ± 24	37 ± 10	14.23 ± 0.21	3.1
Lya 1215	0.30281	122 ± 30	54 ± 6	13.40 ± 0.08	7.7
Lya 1215	0.31512	53 ± 17	18 ± 4	13.07 ± 0.11	4.2
Lya 1215	0.32625	55 ± 11	36 ± 10	13.05 ± 0.09	4.4
Lya 1215	0.33785	54 ± 19	50 ± 4	13.07 ± 0.17	3.6
Lya 1215	0.33923	91 ± 25	66 ± 6	13.28 ± 0.13	4.8
$z = 0.33992 \pm 0.00016$, $\Delta v = 35$ km s^{-1}: $b_{\rm HI} = 27 \pm 7$, log $N_{\rm HI} = 13.02 \pm 0.13$					
Lya 1215	0.33992	51 ± 23	27 ± 7	13.02 ± 0.13	4.2
OVI 1032	0.33989	36 ± 11	9 ± 3	13.59 ± 0.09	4.3
OVI 1038	0.33995	24 ± 14	21 ± 7	13.62 ± 0.10	2.7
Lya 1215	0.36011	66 ± 8	16 ± 3	13.18 ± 0.05	8.0
Lya 1215	0.36129	59 ± 11	49 ± 12	13.06 ± 0.08	5.1
Lya 1215	0.36298	66 ± 11	29 ± 3	13.18 ± 0.09	7.8

Table 2—Continued

Species	$z_{\rm abs}$	W_r (mÅ)	b (km s^{-1})	log N (N in cm^{-2})	SL (σ)
Lya 1215	0.36616	109 ± 12	25 ± 2	13.41 ± 0.04	12.2
$z = 0.36887 \pm 0.00017$, $\Delta v = 37$ km s^{-1}: $b_{\rm HI} = 30 \pm 3$, log $N_{\rm HI} = 13.90 \pm 0.08$					
Lya 1215	0.36887	209 ± 16	28 ± 1	13.82 ± 0.03	13.5
Lyb 1025	0.36883	53 ± 20	33 ± 4	13.90 ± 0.14	6.2
$z = 0.38482 \pm 0.00030$, $\Delta v = 64$ km s^{-1}: $b_{\rm HI} = 43 \pm 1$, log $N_{\rm HI} = 14.10 \pm 0.04$					
Lya 1215	0.38482	362 ± 17	50 ± 1	14.04 ± 0.02	25.4
Lyb 1025	0.38477	92 ± 21	62 ± 5	14.14 ± 0.09	8.9
$z = 0.38583 \pm 0.00026$, $\Delta v = 56$ km s^{-1}: $b_{\rm HI} = 30 \pm 2$, log $N_{\rm HI} = 14.17 \pm 0.03$					
Lya 1215	0.38583	317 ± 16	34 ± 1	14.08 ± 0.02	18.4
Lyb 1025	0.38581	90 ± 5	48 ± 3	14.14 ± 0.03	10.7
Lyg 972	0.38584	32 ± 11	36 ± 12	14.15 ± 0.10	2.2
OVI 1032	0.38569	16 ± 13	29 ± 11	13.13 ± 0.26	2.2
$z = 0.38629 \pm 0.00016$, $\Delta v = 34$ km s^{-1}					
OVI 1032	0.38629	64 ± 12	30 ± 4	13.77 ± 0.06	8.5
OVI 1038	0.38628	25 ± 10	26 ± 7	13.64 ± 0.12	3.3
$z = 0.38660 \pm 0.00022$, $\Delta v = 46$ km s^{-1}: $b_{\rm HI} = 40 \pm 3$, log $N_{\rm HI} = 13.92 \pm 0.12$					
Lya 1215	0.38660	262 ± 25	44 ± 2	13.85 ± 0.04	13.4
Lyb 1025	0.38661	55 ± 32	36 ± 4	13.92 ± 0.19	7.5
OVI 1032	0.38661	118 ± 4	26 ± 1	14.12 ± 0.02	16.6
OVI 1038	0.38662	75 ± 9	26 ± 2	14.16 ± 0.04	10.0
Lya 1215	0.39402	103 ± 24	49 ± 7	13.32 ± 0.08	7.4
$z = 0.40989 \pm 0.00016$, $\Delta v = 34$ km s^{-1}: $b_{\rm HI} = 63 \pm 10$, log $N_{\rm HI} = 13.83 \pm 0.11$					
Lya 1215	0.40989	183 ± 15	48 ± 4	13.62 ± 0.04	12.9
Lyb 1025	0.40973	48 ± 26	77 ± 15	13.83 ± 0.18	4.0
$z = 0.42878 \pm 0.00020$, $\Delta v = 42$ km s^{-1}: $b_{\rm HI} = 24 \pm 6$, log $N_{\rm HI} = 14.03 \pm 0.16$					
Lya 1215	0.42878	246 ± 22	34 ± 1	13.87 ± 0.04	12.4
Lyb 1025	0.42877	61 ± 23	52 ± 7	13.95 ± 0.13	5.0
Lyg 972	0.42876	28 ± 14	47 ± 13	14.14 ± 0.23	2.1
Lyd 949	0.42881	14 ± 84	10 ± 7	14.16 ± 0.13	2.0
Lya 1215	0.43650	113 ± 10	25 ± 2	13.44 ± 0.04	10.4
$z = 0.44099 \pm 0.00032$, $\Delta v = 65$ km s^{-1}: $b_{\rm HI} = 64 \pm 31$, log $N_{\rm HI} = 14.01 \pm 0.10$					
Lya 1215	0.44099	383 ± 28	69 ± 6	14.09 ± 0.06	13.2
Lyb 1025	0.44103	85 ± 18	44 ± 4	14.12 ± 0.08	7.5
Lyg 972	0.44125	16 ± 8	28 ± 10	13.88 ± 0.26	1.9
Lyd 949	0.44081	14 ± 7	15 ± 10	14.18 ± 0.25	1.6
Lya 1215	0.44381	145 ± 32	48 ± 6	13.50 ± 0.07	8.6
$z = 0.47083 \pm 0.00019$, $\Delta v = 38$ km s^{-1}: $b_{\rm HI} = 27 \pm 2$, log $N_{\rm HI} = 13.88 \pm 0.06$					
Lya 1215	0.47083	232 ± 5	29 ± 1	13.88 ± 0.01	7.1
Lyb 1025	0.47093	39 ± 13	25 ± 5	13.77 ± 0.11	4.1
$z = 0.49430 \pm 0.00016$, $\Delta v = 32$ km s^{-1}: $b_{\rm HI} = 58 \pm 1$, log $N_{\rm HI} = 14.01 \pm 0.14$					
Lyb 1025	0.49430	70 ± 23	46 ± 6	14.02 ± 0.12	5.5
Lyg 972	0.49429	24 ± 21	21 ± 5	14.03 ± 0.25	3.4
$z = 0.49568 \pm 0.00016$, $\Delta v = 32$ km s^{-1}: $b_{\rm HI} = 44 \pm 1$, log $N_{\rm HI} = 14.18 \pm 0.14$					
Lyb 1025	0.49568	68 ± 34	63 ± 9	14.00 ± 0.18	4.6
Lyg 972	0.49579	55 ± 18	57 ± 7	14.38 ± 0.12	5.0
$z = 0.58383 \pm 0.00016$, $\Delta v = 30$ km s^{-1}: $b_{\rm HI} = 34 \pm 1$, log $N_{\rm HI} = 14.16 \pm 0.09$					
Lyb 1025	0.58383	80 ± 17	46 ± 7	14.10 ± 0.11	5.1

Table 2—Continued

Species	$z_{\rm abs}$	W_r (mÅ)	b (km s^{-1})	log N (N in cm^{-2})	SL (σ)
Lyg 972	0.58370	73 ± 23	54 ± 7	14.52 ± 0.11	5.3
$z = 0.59602 \pm 0.00018$, $\Delta v = 32$ km s^{-1}: $b_{\rm HI} = 51 \pm 1$, log $N_{\rm HI} = 14.49 \pm 0.02$					
Lyb 1025	0.59602	180 ± 1	44 ± 2	14.52 ± 0.02	10.6
Lyg 972	0.59597	60 ± 33	36 ± 5	14.44 ± 0.19	5.3
Lyd 949	0.59591	19 ± 6	31 ± 5	14.29 ± 0.19	1.8
$z = 0.60355 \pm 0.00016$, $\Delta v = 29$ km s^{-1}: $b_{\rm HI} = 10 \pm 1$, log $N_{\rm HI} = 14.25 \pm 0.10$					
Lyb 1025	0.60355	70 ± 11	14 ± 2	14.15 ± 0.05	6.8
Lyg 972	0.60351	36 ± 10	14 ± 3	14.25 ± 0.08	4.3
Lyd 949	0.60352	13 ± 13	8 ± 7	14.12 ± 0.26	2.0

4. Galaxy Number Density

To assess the number of galaxies along the sightlines toward PKS 1424+240 and 3C66A, we calculate absorber density $\frac{\partial^2 \mathcal{N}}{\partial \log N_{HI} \partial z}$, the number of absorbers contained in intervals of $\log N_{HI}$ to $\log N_{HI} + d \log N_{HI}$, as a function of redshift path length. The process summarized here is detailed in Danforth and Shull (2008). We start by constructing histograms of number of absorbers, binned in 0.5 dex logarithmic column density bins. At lower column densities, instrument resolution defines an upper limit for weak feature detection, leading to an incomplete sample. The COS FUV channels are sensitive to HI absorption of Lyα at $z \leq$0.47 and Lyβ or higher transitions at $0.1 \leq z \leq$0.9. An incompleteness correction is applied by dividing the number, $\mathcal{N}$, per bin by an effective redshift path length, Δz, which is itself a function of column density and accounts for variations in sensitivity to the absorption feature in question. The number density falls off exponentially at higher column densities, so we fit the data with a power law:

$$\frac{\partial^2 \mathcal{N}}{\partial \log N_{HI} \partial z} = C_{14} \left(\frac{N}{10^{14} \mathrm{cm}^{-2}} \right)^{-(\beta - 1)} \tag{3}$$

In which β is the slope and C_{14} is a density normalization constant. The values were then compared to a global fit of $\frac{\partial^2 \mathcal{N}}{\partial \log N_{HI} \partial z}$, calculated from a sample of 75 UV-bright AGN sightlines at $0.058 \leq z_{AGN} \leq 0.852$ and encompassing 2500 absorbers. Uncertainties in $\frac{\partial^2 \mathcal{N}}{\partial \log N_{HI} \partial z}$ were primarily associated with number of absorbers per column density bin stemming from poissonian statistics (Gehrels 1986), along with a small contribution from variation of redshift path length within individual bins. Given the generally poor statistics of analyzing only two sightlines, PKS 1424+240 and 3C66A were combined and fit with a power law as well.

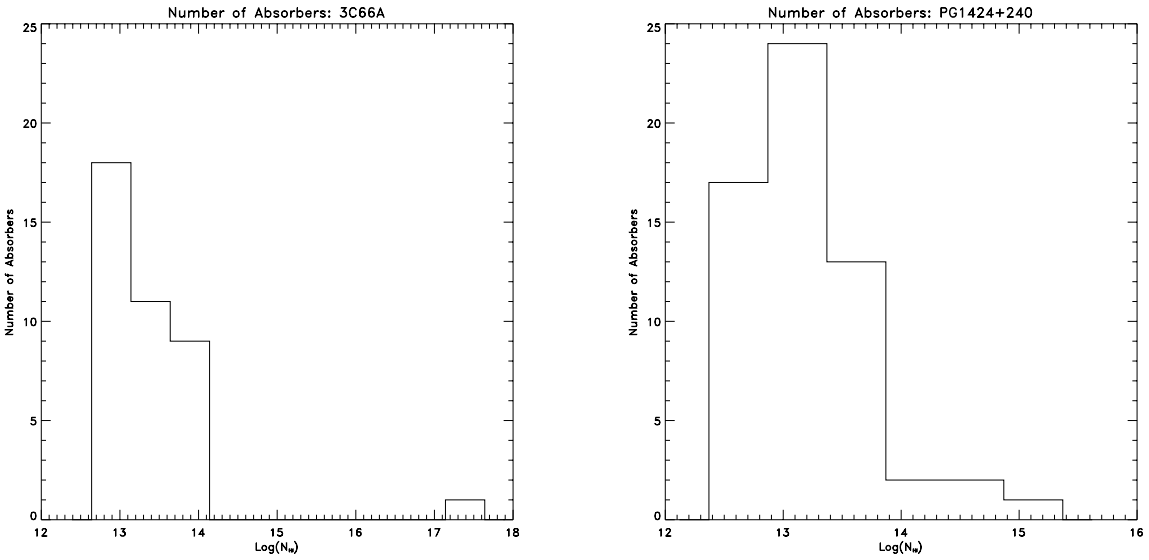

Fig. 2.— Number of absorbers as a function of $\log N_{HI}$ towards individual sightlines 3C66A and PG1424+240

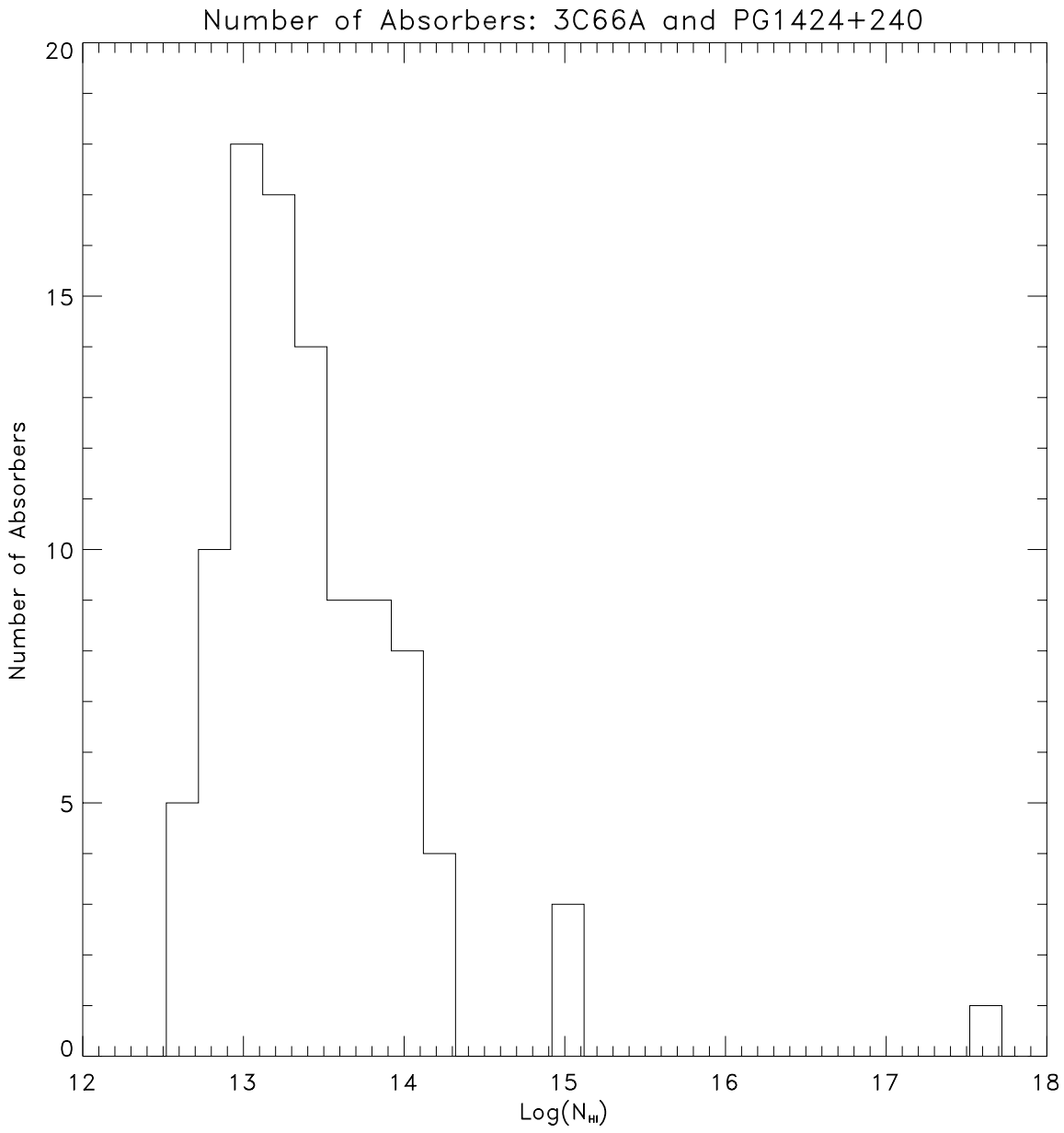

Fig. 3.— Number of absorbers as a function of $\log N_{HI}$ for a combined sample consisting of 3C66A and PG1424+240

Table 3. Galaxy Number Density Power Law Fits

Sightline	Number of Absorbers	Slope β	Offset C14
Global	2508	1.68 ± 0.02	27 ± 1
3c66a	41	1.42 ± 0.11	58 ± 1
PG 1424+240	64	1.76 ± 0.12	40 ± 1
Combined	105	1.56 ± 0.08	47 ± 1

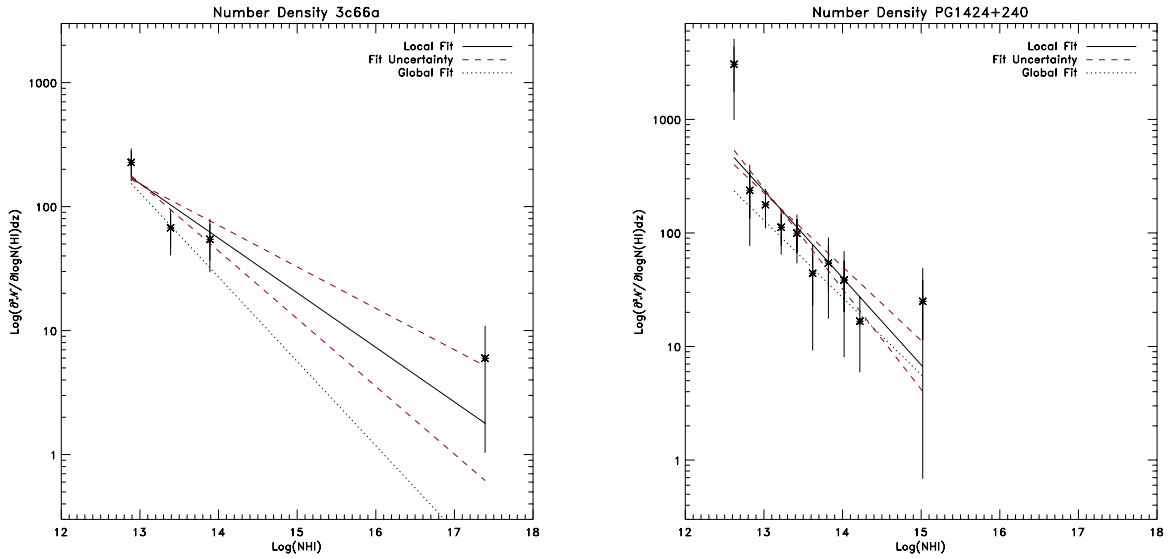

Fig. 4.— Galaxy number density as a function of $\log N_{HI}$ for the sightline towards 3C66A and PG1424+240 individually, fit with a power law and compared to a global sample fit.

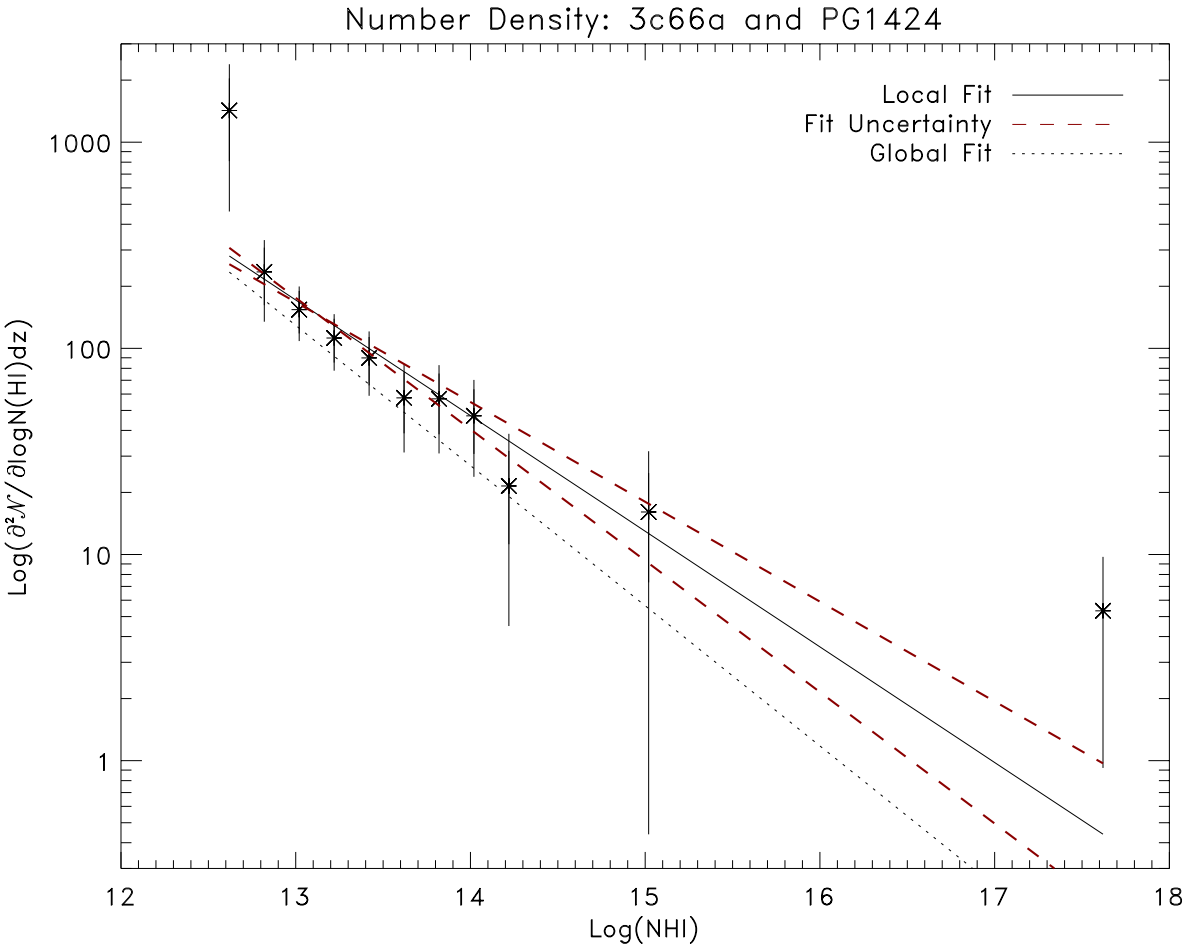

Fig. 5.— Galaxy number density as a function of $\log N_{HI}$ for a combined sample consisting of 3C66A and PG1424+240, fit with a power law and compared to a global sample fit.

We find that power law indicies for each sightline are similar to the global value of $\beta = 1.68 \pm 0.02$, though they fall just short of error bar overlap. A two sample Kolomogorov-Smirnov statistical test on the distribution of column densities for the individual sightlines compared with the global sample resulted in low probabilities of the two samples resulting from the same distribution (3C66A P =0.04, PG1424+240 P =0.003). The combined PG1424+240 and 3C66A absorber distibution, with a value of β =1.56 ± 0.08, is similar in power law index, but shows a higher density (C_{14}) than the global sample. The lack of large deviation from the global sample implies that these sightlines follow a very similar distribution of absorber strengths. However, both of the individual sightlines and the combined sightline have density normalizations approximately twice as high as the global sample, implying that while the column density distribution is similar, the number of absorbers is higher than the global sample average.

5. Relationship Between Column Density and Impact Parameter

In order to gain an understanding of how foreground galaxies that have not been directly observed may be distributed along the line of sight, it is necessary to derive impact parameters from the measured absorption feature properties. Chen et al. (1998) finds a distinct anticorrelation between the strength of neutral hydrogen (equivalent width or column density) absorption and galaxy impact parameter, given in the following relationship:

$$\log\left(\frac{N_{HI}}{10^{20}\mathrm{cm}^{-2}}\right) = -\alpha \log\left(\frac{\rho}{10\mathrm{kpc}}\right) + \beta\left(\frac{L_B}{L^*}\right) + constant \tag{4}$$

where $\alpha = 5.33 \pm 0.50$, $\beta = 2.19 \pm 0.55$, and the constant is 1.09 ± 0.90. Beyond impact parameters, we lack information about the properties of these foreground galaxies. We cannot say anything about galaxy type, orientation of the galaxy in relation to the sightline, or the specific luminosities of each galaxy. Chen et al. (1998) finds no statistically significant dependence of the column density/impact parameter relationship on galaxy inclination, though current observations preclude differentiation of spherical versus flattened disk morphologies. While Chen et al. do find that accounting for B-band luminosity strengthens the relationship between column density and impact parameter, we assert that the flux at the sightline should be nearly independent of individual galaxy luminosity and may thus be ignored by assuming a B-band luminosity of L*. Given that

$$f_\rho = \frac{L}{4\pi\rho^2} \tag{5}$$

We take the logarithm:

$$\log f_\rho = \log L - 2\log\rho - \log 4\pi \tag{6}$$

Then, from equation 4, we isolate a $\log L - 2\log\rho$ term:

$$\log\left(\frac{N_{HI}}{10^{20}\mathrm{cm}^{-2}}\right) = 2.66\left[0.82\left(\frac{L_B}{L^*}\right) - 2\log\left(\frac{\rho}{10\mathrm{kpc}}\right) + 0.41\right] \tag{7}$$

By assuming the luminosity term coefficient of 0.82 is approximately 1 (a value within the error bars of equation 4), we rearrange equation 6 to get

$$\log f_\rho = \frac{\log N_{HI}}{2.66} - 0.7 \tag{8}$$

Thus the nearest galaxy flux at the inferred impact parameter is most strongly correlated with the observed neutral hydrogen column density measured at ρ. This parameterization estimates the flux f_ρ from N_{HI}. Since f_ρ is independent of galaxy luminosity, we assign a fiducial luminosity of L* to estimate ρ.The following tables list the impact parameters ρ for foreground Lyman α absorbers, assuming a nearest galaxy luminosity of L*.

Table 4. Impact Parameters of Absorption Systems Towards 3C66A

Redshift	$\log N$ cm^{-2}	ρ kpc	Redshift	$\log N$ cm^{-2}	ρ kpc
0.01991	13.08 ± 0.11	318 ± 15	0.16240	13.37 ± 0.03	281 ± 4
0.02028	13.01 ± 0.09	328 ± 13	0.16964	13.01 ± 0.06	328 ± 8
0.02730	13.47 ± 0.04	269 ± 5	0.17519	13.60 ± 0.03	254 ± 3
0.04254	13.29 ± 0.04	291 ± 5	0.17516	13.72 ± 0.15	241^{+15}_{-16}
0.04424	13.18 ± 0.06	305 ± 8	0.17563	14.15 ± 0.01	200 ± 1
0.05122	13.89 ± 0.04	224 ± 4	0.17563	14.45 ± 0.06	176 ± 5
0.05150	13.75 ± 0.05	238 ± 5	0.17565	14.55 ± 0.01	169 ± 1
0.05341	13.21 ± 0.05	301 ± 6	0.18942	13.23 ± 0.05	298 ± 6
0.06710*	13.69 ± 0.04	239 ± 3	0.22820	12.89 ± 0.13	345^{+19}_{-20}
0.06750*	17.64 ± 0.12	154 ± 3	0.22859	13.61 ± 0.04	253 ± 4
0.07974	13.65 ± 0.02	248 ± 2	0.23408	13.34 ± 0.06	284 ± 7
0.08020	12.96 ± 0.11	335 ± 16	0.24230*	14.16 ± 0.02	203 ± 2
0.08346	13.35 ± 0.04	283 ± 4	0.24270*	13.83 ± 0.04	229 ± 2
0.08872	14.32 ± 0.03	186 ± 2	0.26111	13.79 ± 0.19	234^{+18}_{-20}
0.10824	13.10 ± 0.06	315 ± 8	0.26125	13.57 ± 0.10	257 ± 11
0.11550	14.08 ± 0.01	207 ± 1	0.29268	13.14 ± 0.12	310 ± 16
0.11546	14.35 ± 0.22	184^{+17}_{-18}	0.29906	13.26 ± 0.08	294 ± 10
0.12027	12.98 ± 0.07	332 ± 10	0.30060*	13.67 ± 0.05	241 ± 5
0.13051	13.03 ± 0.08	325 ± 11	0.30090*	13.75 ± 0.04	248 ± 4
0.13062	13.94 ± 0.10	219 ± 9	0.32830*	14.24 ± 0.01	186^{+21}_{-23}
0.14187	13.33 ± 0.05	286 ± 6	0.33329	14.14 ± 0.03	201 ± 3
0.15160*	13.90 ± 0.05	218 ± 8	0.33321	14.25 ± 0.08	192 ± 7
0.15180*	13.94 ± 0.10	216 ± 6	0.33318	14.32 ± 0.24	186^{+18}_{-20}
0.15184	13.94 ± 0.10	219 ± 9	0.33322	14.23 ± 0.38	194^{+29}_{-35}
0.15186	14.02 ± 0.18	212^{+16}_{-17}	0.33476	13.71 ± 0.05	242 ± 5
0.15205	13.57 ± 0.22	257^{+23}_{-26}	0.33473	13.62 ± 0.32	252^{+32}_{-37}
0.15210*	13.57 ± 0.22	292 ± 5			

*Absorbers for which metal ions were also detected.

Table 5. Impact Parameters of Absorption Systems Towards PG1424+240

Redshift	$\log N$ cm^{-2}	ρ kpc	Redshift	$\log N$ cm^{-2}	ρ kpc
0.01747	13.55 ± 0.03	260 ± 3	0.28525	14.29 ± 0.11	189 ± 9
0.01877	14.32 ± 0.03	186 ± 2	0.28524	14.23 ± 0.21	194^{+17}_{-18}
0.01917	13.32 ± 0.07	287 ± 9	0.30281	13.40 ± 0.08	277 ± 9
0.02000	12.80 ± 0.09	359 ± 14	0.31512	13.07 ± 0.11	319 ± 15
0.03908	13.15 ± 0.28	309^{+35}_{-40}	0.32625	13.05 ± 0.09	322 ± 13
0.04117	13.45 ± 0.04	271 ± 5	0.33923	13.28 ± 0.13	292^{+16}_{-17}
0.05072	13.22 ± 0.09	299 ± 12	0.33990*	13.13 ± 0.06	311 ± 8
0.06162	13.30 ± 0.06	289 ± 7	0.36011	13.18 ± 0.05	305 ± 7
0.08328	13.40 ± 0.17	277^{+20}_{-21}	0.36129	13.06 ± 0.08	321 ± 11
0.08339	13.09 ± 0.19	317^{+25}_{-27}	0.36298	13.18 ± 0.09	305 ± 12
0.10584	13.60 ± 0.03	254 ± 3	0.36616	13.41 ± 0.04	276 ± 5
0.11584	14.39 ± 0.08	181 ± 6	0.36887	13.82 ± 0.03	231 ± 3
0.11966	13.35 ± 0.05	283 ± 6	0.36883	13.90 ± 0.14	223 ± 13
0.12130*	15.11 ± 0.10	136 ± 2	0.38477	14.14 ± 0.09	201 ± 8
0.12537	13.47 ± 0.08	361^{+23}_{-24}	0.38482	14.04 ± 0.02	210 ± 2
0.12753	13.47 ± 0.08	269 ± 9	0.38580*	14.17 ± 0.10	199 ± 9
0.12768	13.89 ± 0.05	224 ± 5	0.39402	13.32 ± 0.08	287 ± 10
0.12776	13.84 ± 0.04	229 ± 4	0.40989	13.62 ± 0.04	252 ± 4
0.12768	13.89 ± 0.05	224 ± 5	0.40973	13.83 ± 0.18	230^{+17}_{-19}
0.13325	13.51 ± 0.04	264 ± 5	0.42878	13.87 ± 0.04	226 ± 4
0.13634	13.23 ± 0.13	298^{+16}_{-17}	0.42877	13.95 ± 0.13	218 ± 12
0.14537	13.09 ± 0.06	316 ± 8	0.42876	14.14 ± 0.23	201^{+19}_{-21}
0.14680*	14.50 ± 0.08	172 ± 6	0.42881	14.16 ± 0.13	199 ± 11
0.14720*	15.16 ± 0.11	129 ± 6	0.43650	13.44 ± 0.04	272 ± 5
0.14796	13.49 ± 0.06	266 ± 7	0.44099	14.09 ± 0.06	206 ± 5
0.15868	12.94 ± 0.08	338 ± 12	0.44103	14.12 ± 0.08	203 ± 7
0.17250	12.76 ± 0.29	365^{+43}_{-49}	0.44125	13.88 ± 0.26	225^{+24}_{-27}
0.17838	13.50 ± 0.02	265 ± 2	0.44081	14.18 ± 0.25	198^{+20}_{-23}
0.18035	12.87 ± 0.10	348 ± 15	0.44381	13.50 ± 0.07	265 ± 8
0.18811	13.21 ± 0.08	301 ± 10	0.47083	13.88 ± 0.01	225 ± 1
0.18902	12.83 ± 0.07	354 ± 11	0.47093	13.77 ± 0.11	236 ± 11
0.20040*	14.55 ± 0.11	169 ± 8	0.49430	14.02 ± 0.12	212 ± 11
0.20080*	14.82 ± 0.15	150 ± 10	0.49429	14.03 ± 0.25	211^{+22}_{-24}
0.20640	13.79 ± 0.01	234 ± 1	0.49568	14.00 ± 0.18	214^{+16}_{-17}
0.20651	13.63 ± 0.41	251^{+41}_{-49}	0.49579	14.38 ± 0.12	181 ± 9
0.21208	12.62 ± 0.15	388^{+24}_{-26}	0.58383	14.10 ± 0.11	205 ± 10
0.23090	12.74 ± 0.09	368 ± 14	0.58370	14.52 ± 0.11	171 ± 8
0.24159	12.98 ± 0.07	332 ± 10	0.59602	14.52 ± 0.02	171 ± 1
0.25025	13.70 ± 0.02	243 ± 2	0.59597	14.44 ± 0.19	177^{14}_{15}
0.25031	13.76 ± 0.26	237^{+25}_{-28}	0.59591	14.29 ± 0.19	189^{+15}_{-16}
0.26634	13.14 ± 0.06	310 ± 8	0.60355	14.15 ± 0.05	200 ± 4
0.28005	13.16 ± 0.19	307^{+24}_{-26}	0.60351	14.25 ± 0.08	192 ± 7
0.28519	13.93 ± 0.07	220 ± 7	0.60352	14.12 ± 0.26	203^{+22}_{-24}
0.28536	14.04 ± 0.02	210 ± 2			

*Absorbers for which metal ions were also detected.

For a limiting N_{HI} set by the spectrum, at a given galaxy luminosity (L*, 0.1 L*, 0.01 L*, etc) a search volume with radius $\rho\,(L*)$, $\rho\,(0.1L*)$, $\rho\,(0.01L*)$, etc will contain one galaxy for each Lyα absorber in the FUV spectra. Therefore a galaxy luminosity function may be used to obtain a rough galaxy density along the line of sight. This may then be compared to the observed global luminosity function.

6. Luminosity Functions

The luminosity function provides a second probe of the foreground absorber population. From Schecter (1976), we have an analytic luminosity function for number of galaxies per luminosity interval:

$$\phi(L)dL = \phi^* \left(\frac{L}{L^*}\right)^{\alpha} e^{-\left(\frac{L}{L*}\right)} d(L/L^*) \tag{9}$$

Where ϕ* is a space density constant in Mpc^{-3}. We assume that a system of lines at the same redshift and with HI column densities greater than 10^{14} cm^{-2} indicates the presence of a foreground galaxy. We assume a fiducial luminosity value for each galaxy of L*. The cylindrical volume over which ϕ* is calculated is determined by the distance to the blazar and the largest impact parameter along the sightline. At higher redshifts, instrument sensitivity limits detection of lower column densities, thus we shrink our cylindrical radius to the largest impact parameter of 10^{14} cm^{-2} absorbers after the redshift at which no more 10^{13} cm^{-2} absorbers are detected. This cutoff applied to the more distant PG1424+240, at $z \sim 0.47$. We then divide the number of absorbers greater than 10^{14} cm^{-2} by the total composite cylindrical volume: 635 Mpc^3 for 3C66A and 746.9 Mpc^3 for PG1424+240. This process was repeated to include absorbers greater than 10^{13} cm^{-2}. All calculations assume $H_0 = 70$ km s^{-2} Mpc^{-3} and a poissonian error was applied to the absorber numbers.

Table 6. Luminosity Function Space Density Constants

Sightline	Absorbers $>10^{14}\mathrm{cm}^{-2}$	ϕ* Mpc^{-3} $>10^{14}\mathrm{cm}^{-2}$	Absorbers $>10^{13}\mathrm{cm}^{-2}$	ϕ* Mpc^{-3} $>10^{13}\mathrm{cm}^{-2}$
Global*		4.5×10^{-3}		
3c66a	10 ± 4	$(1.6 \pm 0.6) \times 10^{-2}$	41 ± 7	$(6.5 \pm 0.1) \times 10^{-2}$
PG 1424+240	15 ± 5	$(2.0 \pm 0.7) \times 10^{-2}$	64 ± 9	$(8.6 \pm 0.1) \times 10^{-2}$

*Calculated in Stocke et al. 2013

The space density constants for absorbers greater than 10^{14} cm^{-2} for both 3C66A and PG1424+240 are approximately three to four times greater than the global average. This result implies that the two sightlines are much denser than the average sightline. When absorbers in the $\geq 10^{13}$ cm^{-2} regime are considered, the space density constant increases by roughly 20%.

7. Conclusions

The data indicate that these two sightlines are unexpectedly dense in galactic absorbers, which is at odds with the prediction that lower absorber densities cause lowered gamma ray opacity and thus TeV gamma ray detection beyond the predicted EBL redshift horizon. Both the $\frac{\partial^2 \mathcal{N}}{\partial \log N_{HI} \partial z}$ values and the luminosity ϕ^* star values are higher than global measurements, suggesting more absorbers than the average sightline.

This unexpected result implies that our understanding of TeV gamma ray propagation is still flawed. These flaws are most likely in the EBL models, which depend on uncertain assumptions like intrinsic blazar spectrum, star formation rates, galactic emissivities, and galactic evolution models. Especially in the infrared regime of the EBL SED, the poor statistics of galaxy detection in deep surveys render accurate EBL modeling difficult. However, more exotic physics may also play a role in the limitation of gamma ray attenuation. Unconfirmed particles like axions (Sanchez-Conde 2009) or hidden photons (Zechlin 2008) are predicted to prevent VHE gamma ray absorption (Kneiske 2010).

Given the poor statistics of only two sightlines to analyze, future work should center on identifying additional anomalously high redshift TeV-bright blazar sightlines and obtaining high quality FUV spectra of these objects. One such object is already known. Blazar 3C279, a TeV source at $z \sim 0.536$, is a prime candidate for reobservation with HST/COS or future UV spectrographs, as existing observations from HST/FOS do not exhibit the resolution necessary to distinguish Lyman α forest lines at column densities of 10^{14} cm^{-2} for this type of sightline analysis. Furthermore, probing the nature of the foreground absorbers using photometric or spectroscopic techniques may also elucidate anomalies in these sightlines.

REFERENCES

Acciari, V. A., et al., 2009, ApJ, 720, 1174

Acciari, V.A., et al., 2010, ApJ, 708, 100

Aharonian, F., et al., 2006, Nature,440, 1018

Chen, H. W., et al. 1998, ApJ, 498, 77-94

Chen, H. W., 2012, MNRAS, 427. 1238

Danforth, C.W. & Schull, J.M., 2008, ApJ, 679, 194

Danforth, C.W., 2010, ApJ, 720, 976

Danforth, C.W., 2014, ApJ, submitted, arXiv:1402.2655

Furniss, A., et al. 2013, ApJ, 766, 35

Furniss, A., et al. 2013, ApJ, 768, 31

Gehrels, N., 1986, ApJ, 303, 336

Kneiske, T. M., Mannheim, K.,& Hartmann, D.,2002, ApJ, 386, 1

Kneiske, T. M. & Dole, H., 2010, A&A, 515, A19

Neshpor, Y.I., et al., 1998, AstL, 24, 134N

Primack, J., 2005, AIPC, 745, 23

Sanchez-Conde, M.A., et al, Phys.Rev.D, 79, 123511

Schecter, P., 1976, ApJ, 203, 297

Stecker, F. W., de Jager, O. C., 1993, ApJ, 415,71S

Stecker, F.W., Malkan, M.A., & Scully, S.T., 2006, ApJ, 648, 774

Stocke, J.T., et al., 1998, AJ, 115, 451-459

Stocke, J., Danforth, D., & Perlman, E., 2011, ApJ, 732, 113

Stocke, J.T., et al., 2013, ApJ, 763, 148

Zechlin, H.S., et al., 2008, AIPC, 1085, 727